International Journal of Bioprinting

RESEARCH ARTICLE

Monolayer heterojunction interactive hydrogels for high-freedom 4D shape reconfiguration by two-photon polymerization

Yufeng Tao[1,2]*, Chengchangfeng Lu[3], Xuejiao Wang[1], Zhiduo Xin[1], Xia Cao[1]*, Yunpeng Ren[1]

[1]Institute of Micro-nano Optoelectronics and Terahertz Technology, Jiangsu University, Zhenjiang, 212 013, China

[2]Wuhan National Laboratory for Optoelectronics, Huazhong University of Science and Technology, Wuhan, 430 074, China

[3]Whiting School of Engineering, Johns Hopkins University, Baltimore, 21218-2688, U.S.A.

Abstract

Mimicking natural botanical/zoological systems has revolutionarily inspired four-dimensional (4D) hydrogel robotics, interactive actuators/machines, automatic biomedical devices, and self-adaptive photonics. The controllable high-freedom shape reconfiguration holds the key to satisfying the ever-increasing demands. However, miniaturized biocompatible 4D hydrogels remain rigorously stifled due to current approach/material limits. In this research, we spatiotemporally program micro/nano (μ/n) hydrogels through a heterojunction geometric strategy in femtosecond laser direct writing (fsLDW). Polyethylene incorporated N-isopropylacrylamide as programmable interactive materials here. Dynamic chiral torsion, site-specific mutation, anisotropic deformation, selective structural coloration of hydrogel nanowire, and spontaneous self-repairing as reusable μ/n robotics were identified. Hydrogel-materialized monolayer nanowires operate as the most fundamental block at nanometric accuracy to promise high freedom reconfiguration and high force-to-weight ratio/bending curvature under tight topological control. Taking use of this biomimetic fsLDW, we spatiotemporally constructed several in/out-plane self-driven hydrogel grippers, diverse 2D-to-3D transforming from the same monolayer shape, responsive photonic crystal, and self-clenched fists at μ/n scale. Predictably, the geometry-modulable hydrogels would open new access to massively-reproducible robotics, actuators/sensors for microenvironments, or lab-on-chip devices.

Keywords: Interactive hydrogel; Heterojunction nanostructures; Spatiotemporal programming; Chiral torsion; High freedom

***Corresponding author:**
Yufeng Tao
(*Taoyufeng@ujs.edu.cn*)
Xia Cao
(*Caoxia@ujs.edu.cn*)

Citation: Tao Y, Lu C, Wang X, *et al.* 2023, Monolayer heterojunction interactive hydrogels for high-freedom 4D shape reconfiguration by two-photon polymerization. *Int J Bioprint,* 9(3): 678. https://doi.org/10.18063/ijb.678

Received: August 22, 2022

Accepted: October 21, 2022

Published Online: February 3, 2023

1. Introduction

Shape-reconfigurable materials have evolved ubiquitously in the nature, encompassing the living organism, plants, muscles, and peristaltic cells, featuring high-strength, and multi-dimensional shape reconfiguration over its long history[1]. For instance, plants utilize water-sorption-to-desorption for morphogenesis, and a blooming flower changes its petals curvature in a few hours or days[2]. Flytrap snaps at ultrafast speed to switch its

curvature by releasing turgor across the leaf[3]. *Antheraea pernyi* silk fiber contracts and combines amorphous silk fibers, which spin into crystallization for tough silk fibers. Shape-reconfigurable materials have inspired intensive effort in bioscience[4], automatic robots/organ regeneration[5], self-deployed components/actuators[6,7], and even self-adaptive optics/photonics[8] without joints or hinges. The self-driven structural reorganization becomes a new frontier of current four-dimensional (4D) prototyping and manufacturing.

Soft-interactive hydrogels[9] have been regarded as the most promising self-driven robotics[10], which render stationary three-dimensional (3D) structures with morphological mutation[11] by small loads of stimuli, possessing desirable ductility, biocompatibility, optical clarity, lightweight, and easy synthesis (Table S1)[12-16]. To date, our literature review confirms several pioneered hydrogel artificial grippers[12], self-perspiring actuators[13,14], deployable cages or scaffolds[15,16], drug delivery[17], tissue regeneration[5], adaptive optics/photonics[8], simple microrobot collector[19], and soft machines[20,21]. However, there are some intrinsic bottlenecks of massively applying hydrogels originating from their sluggish expansion or poor controllability in direction/stiffness[22,23] due to the isotropic shape reconfiguration. Macroscopic 4D biomimetic hydrogels using inks are still at an early stage and are physically inaccessible to microenvironments of lab-on-chip devices[24], microbiological tissues (blood vessel, capillary, or artery)[25], or micro/nano (μ/n) electromechanical systems because of bulky volume and poor volumetric programming resolution. Therefore, it is strategically important for miniaturizing the self-driven 4D hydrogels at high resolution and high shape controllability to develop embedded bio-applications.

The last decade witnessed significant strides in two-photon polymerization (TPP)[26,27] toward on-demand 4D μ/n applications. Despite the progress, high-freedom shape reconfigurations remain a formidable prerequisite for practical robotics. The intensively-used stress-releasing method[28] generates only unidirectional deformations without resilience. TPP fabrication of compound machines[15,18] necessitates tedious preparation/scanning steps, increasing time/material cost to hinder producibility. Unfortunately, weak interfacial coupling between multi-layers leads to mechanical mismatch and low strengths. To substantially overcome these limitations, we upgrade the shape controllability (Figure 1) by monolayer heterojunction scanning for biomimetic reversible multi-dimensional shape reconfiguration. Here, the conventional femtosecond laser direct writing (fsLDW) procedure was facilitated by incorporating hydrogel-nature materials[29-33], and as obtained, became enabled to trigger a series of versatile high-freedom 4D behaviors at nanometer accuracy.

Herein, triallyl isocyanurate (TAIC), a biocompatible crosslinking agent, strengthens the polymeric bonding between extender N-isopropylacrylamide (NIPAM)[34,35] and polyethylene glycol-diacrylate (PEG-DA)[24,33] (Figure S1) due to their desirable miscibility. The monolayer nanostructured interactive hydrogels (MNIHs) were a composite network of NIPAM/PEG showing amphiphilicity, enhanced responsiveness, and desirable structural integrity. A cationic photoinitiator (methylene blue[36], MB, a derivative of phenothiazine with a high photon absorption ratio[37]) triggers the confined two-photon polymerization (TPP)[27] in a sub-micrometer laser-focus voxel (Videoclip S1) at tunable optical parameters (Table S2). MNIHs featured hierarchical polymeric degrees, succeeding in harnessing tunable mechanics[38,39] at high-order directions much better than the reported isotropic PNIPAM hydrogels. Our home-built mask-free transfer-free fsLDW system[40,41] fully utilized the hydrogel's properties[42-45] owing to higher-complexity shape morphing function at ultrafine resolution. fsLDW-fabricated MNIHs exhibited self-driven high freedom contraction, torsional twisting, reverse distortion, large-angle rotations, directional gripping, and structural coloration, and allowed researchers to select stimuli. Some physically-damaged MNIHs recovered themselves like having self-consciousness, ensuring long-term use for extreme conditions. To simplify the discussion, all hydrogels at μ/n footprint were rapidly prepared using fsLDW, and referred to as MNIH.

2. Materials and methods

2.1. Precursor preparation

As illustrated in Figure S1, NIPAM ($C_6H_{11}NO$, 0.6696 mg, 99.99+% purity, Mw = 113.16, extender), PEG-DA ($(C_3H_3O).(C_2H_4O)n.(C_3H_3O)$, 1.8 mL, 99.999+% purity, Mw = 700, crosslinker) were added to potassium persulfate ($K_2S_2O_8$, 0.001 mg, Mw = 270.32) for a room-condition pre-polymerization. Subsequently, TAIC ($C_{12}H_{15}N_3O_3$, Mw = 249.27, a crosslinking agent, 0.04 mg) was ground and added into the mixture with MC ($C_{16}H_{18}ClN_3S$), and then vortexed and sonicated to homogenous precursor; sediment was removed before fsLDW (Figure S1). The precursor-containing materials were obtained commercially and used without further purification.

2.2. Morphological characterization

The indium tin oxide (ITO)-coated glasses operated as the substrates for the as-fabricated MNIHs, which provided a

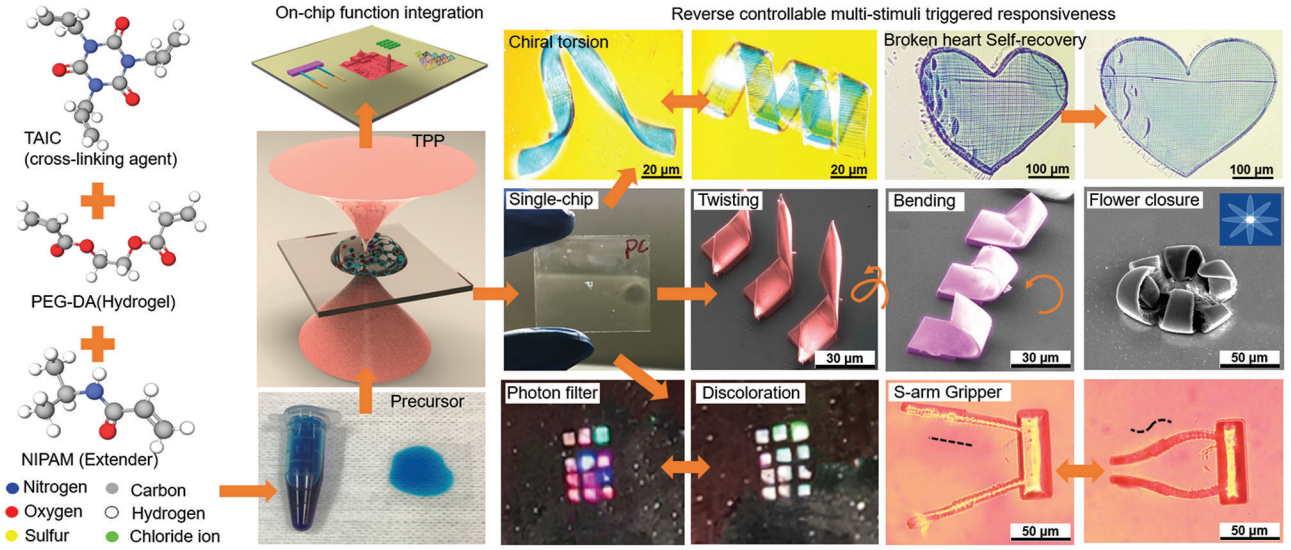

Figure 1. The schematic flowchart begins with facile preparation of homogeneous responsive precursors (mixed PEG-DA, NIPAM, MB, and TAIC in polyethylene glycol), followed by a biomimetic femtosecond laser direct writing method scanning at a pre-designed path to generate high-fidelity function-controllable monolayer nanostructured interactive hydrogels (MNIHs), subsequently, the residual precursor solution was rinsed off, and MNIHs were loaded stimuli for high-kinematic shape reconfiguration

conductive background for scanning electron microscopy (SEM) images or secondary-electron images. Besides the Olympus digital microscopes, 3D micrographs of the shape-reconfigured MNIHs were achieved by utilizing a laser scanning confocal microscope (LSCM, VK-X1000, Keyence) to digitally reconstruct the sample profile at nanometer accuracy (shown in Supplementary File). Geometric parameters were figured out by the Keyence analysis software.

2.3. Two-photon polymerization

TPP was done by a femtosecond laser system on isolating optical platform to realize monolayer heterojunction hydrogel. The laser system contained Ti: sapphire laser (density of optical power ranges from 2 to 20 mW/μm^{-2}). A 2D galvanometer cooperated with one longitudinal translation platform to realize 3D trajectories (Videoclip S1). A self-developed analysis software converted stereolithography file (STL) of models into structure data and directed the movement of laser focus. The focused oil objective provided ultra-precise feature sizes down to 180 nm confined inside the laser focus voxel using the hydrogel-nature precursors.

2.4. Thermogravimetric analysis (TGA)

We conducted TGA to estimate the dynamic solvent retention of MNIHs affected by temperature. The TGA analyzer (Q500, TA Instruments) adjusted the ambient temperature inside the chamber at the vacuum degree of 100 torr. The pure PEG-DA hydrogel was compared with the composite MNIHs here. The equipped precise scale reflected the mass changes at a resolution of <0.1 μg. Solvents inside fully-swelled MNIHs were gradually evaporated in TGA tests when the ambient temperature increased at a step of 5°C/min at the range of 30°C – 60°C by infrared heating. The relative mass loss was calculated at $(m_{initial}\text{-}m_{real})/m_{initial}$ to reflect the water retention of MNIHs. The dehydration speed of water was calculated by differential operation on mass loss along time.

2.5. Cell cytotoxicity tests

The as-fabricated MNIH samples (one PC sample and one hollow scaffold) were first disinfected and then added cell culture medium placed in a non-dust room. The used cell culture medium contained small ratios of amino acids, glucose, vitamins, and trace elements for fibroblast cell's survival and reproduction. A fluorescence microscope (Nikon Ti-U) reflected and summarized the cell activities over two weekends as experimental verification of cytocompatibility. The viability of fibroblasts was examined using the live-dead assay kit (Abcam, ab115347), and the ratios of live/dead cells were calculated with Image J.

2.6. Optical spectroscopic investigation

To interpret the process of TPP-induced molecular linking, we conducted Fourier-transform infrared (FTIR) spectroscopic observation on MNIHs and precursor material compositions. The FTIR spectra were read by Nicolet ™ nexus670 to reflect the molecule structural transfer. Another optical spectrograph (SCT-320,

Princeton) was used to detect the transmission/reflection spectra of each PC sequentially for coloration at a resolution of 0.2 nm. All optical observation or CCD profiling was done by the digital microscope terminal of the laser system (X81, Olympus).

2.7. Micromechanics test

In this case, a micromechanics tester (FT-MTA02) from FemtoTools measured MNIH samples at the vertical and horizontal axes to detect stiffness/Young's modulus, cohesive behavior, and output force amplitude. The equipped Tungsten probe, which records the generated compressive and tensile force, was waterproof for contacting with solvents at a micrometer tip radius (a fraction of 2 μm).

3. Results and discussion

The self-driven high-freedom MNIHs combined with edgy femtosecond laser fabrication technique and advanced material sciences were studied via necessary characterization methods here. Surficial functional groups of MNIH matrix spontaneously perceived stimuli, interacted with organic matters or ions for diffusion, or were remotely activated by light/heat radiation to transfer heat. First, we freeze-dried a cantilever beam to observe molecular-chain conformation. The linked network exhibited an interlaced, bumpy, nanofibrous tangled conformation (Figure 2) instead of a stereotypical porous network of hydrothermal synthesized PNIPAM, offering a sizeable contact area to load stimuli. Subsequently, we conducted FTIR spectroscopic observation (Figure 2B, laser wavelength 532 nm, optical power 1 mW, and wavenumber range from 500 to 4000 cm^{-1}) to deduct molecular structural transferring. MNIH spectrum contained the absorption peaks of amide bond (C=O at 1654.2 cm^{-1}, N-H at 1560.1 cm^{-1}) from NIPAM, accompanied by ester structure of PEG-DA (C-O at 1160.2 cm^{-1}). It could be understood that MNIH was crosslinked by NIPAM and PEG-DA in pre-polymerization and TPP.

In situ micromechanics measurements (using FT-MTA02, FemtoTools, with 2-μm radius tungsten probes and capacitive force sensor were used in the loading/unloading process at 5 nN resolution, Figure 2C) elucidated the MNIHs' elasticity, guaranteeing structural integrity during violent mutation, which was pivotal to addressing challenges in bio-interconnects and soft machines/robots. We further identified the generated internal stress, stiffness, and adhesion by circles of penetrating-in (compressive) and pulling-out (tensile) operations. Stiffness of swelled MNIHs (<300 N/m) increased to >4,000 N/m after drying, implying tunable Young's modulus range[38,39] (from <10 MPa immersed in ethanol to >55 MPa after dehydration, Figure S3) well-suited for device-level applications. The force-to-weight ratio exceeded 1000 N/mg tested on MNIHs. The relation of stress (load force) and displacement exclusively presented variable hysteresis loops, validating that MNIHs had at least two metastable phases while interacting with stimuli.

Hydrophilicity/hydrophobicity switch of pure NIPAM happened at its lower at the lower critical solution temperature ($LCST_{NIPAM}$=32.4°C, Figures S4 and S5)[21], however, the hydrophilicity/hydrophobicity switch of MNIH extended to more broad 30 – 42°C zone[21]. In addition, amphiphilicity of PEG-DA[24] offered another privilege to interact with oils, acrylates, and organic polar solvents (such as DMSO, and IPA.), far beyond the single water/humidity for shape mutation (Figure 2D). Subsequently, based on the experiment, we concluded that the material ratio affected the water-contact angle (Figure 2E) noticeably, and the contact angle declined in the order of 63.35°→56.49°→46.25°→37.87°, which was ascribed to the increased NIPAM: PEG-DA ratio in the order of 0.5:1→1:1→2:1→3:1. In the respect to shape reconfiguration, we numerically investigated a model on cantilever beam shape through finite element framework (Figures 2F and S6), 3D stress distribution confirmed that the interconnecting arm released the mechanical energy accumulated from the intermolecular force, and the fixation pads bore the maximum residual stress, matching with the beam's upward humping as described in SEM images (Figure 2F).

To meticulously regulate the spontaneous interaction between MNIHs and stimuli, we introduced a monolayer heterojunction nanostructure (Figure 3) based on nanowires (NWs) by our high-precision laser scanning method[40], modulating NWs' interspacing and line width. After polymerization, the solidified NWs worked as a skeleton, and the loosely-linked interspacing provided unfolding space and a large quantity of survived functional groups. NWs connected each other through interspacing, forming a high-quality monolayer hierarchical heterojunction at tight topological control. After simplifying the scanning path, we succeeded in manipulating the μ/n-scale mutation behaviors to break the freedom constraints of conventional methods (Videoclips S2 and S3). The first evidence, a transparent "bracelet" (Figure 3A) with a horizontal expansion >120%, lateral growth <8%, a longitudinal expansion >110%, and a curvature radius of 32 μm, was reversely constructed from a simple monolayer planar MNIH (dimensions of 30 × 150 × 4 $μm^3$).

Beyond this common conformal bending/extension, the unique chiral torsional spirochete, which received ever-increasing attention recently, was facilely reconstructed.

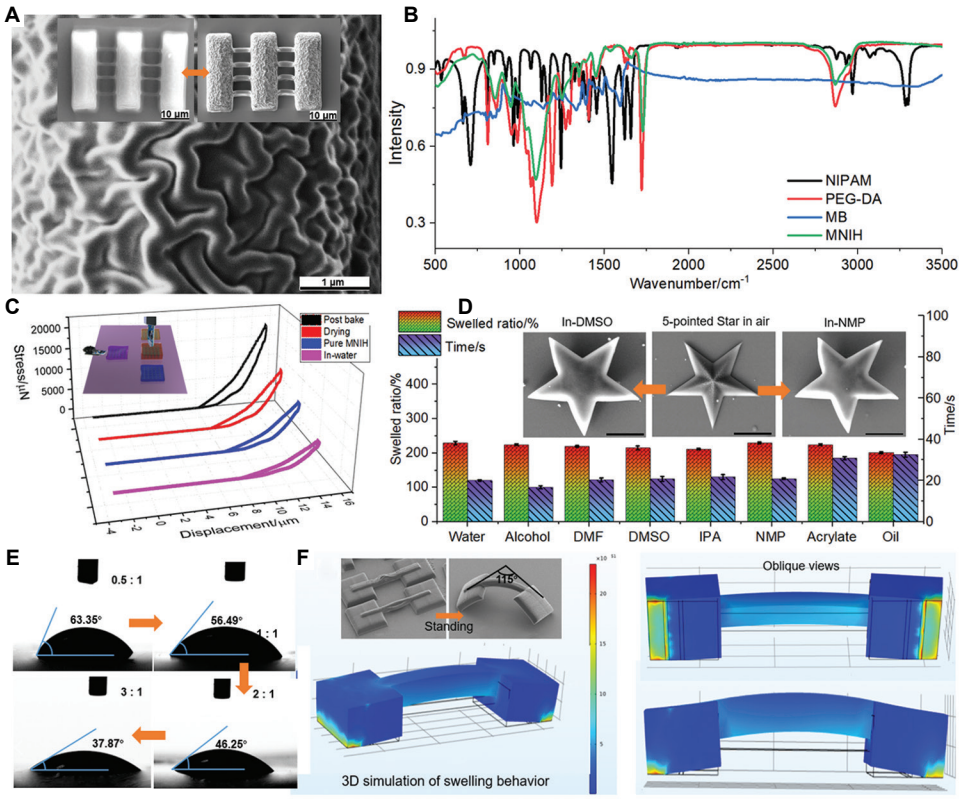

Figure 2. (A) Inset figures display the laser-scanned cantilevers equilibrium, swelled and dried respectively. The zoomed-in SEM image exhibited an intertwined 3D matrix. (B) Normalized FTIR spectra of precursor compositions and MNIHs, where PEG-DA spectrum displayed =C-H stretching vibration (2970.1 cm^{-1}), a strong absorbing spectrum of ester bond C=O (1728.9 cm^{-1}). NIPAM spectrum manifested the stretching vibration of N-H in acylamino (3283.2 cm^{-1}), C-H deformation vibration, and a stretching vibrational peak of C-O in ester (1367.5 cm^{-1}). (C) Inset illustration shows mechanical tests on the nano-indentation principle, and the representative hysteresis loops imply the elasticity of hydrogel nature, which changes the loop shape at different states. (D) The swelling ratios of MNIH absorbed different chemicals. (E) Dynamic water contact angles on the surfaces at varied material ratios. (F) Inset SEM images show a hydrogel cantilever standing out from the substrate. 3D illustrations are finite element calculations to verify the shape-morphing trends and stress, matching the practical results

We intentionally tilted the scanning direction (Figure 3B) in forming the same planar, which transformed into a spirochete, rotated at three turns, otherwise, opened, and restored to its original shape as a chiral torsion (Videoclip S2) in an oblique view and optical microscope images. Mechanics tests found the lateral swelling force exceeding 10 N at a small footprint area of 50 × 500 μm^2, repeated deformation manifested a slight deviation of smaller than 5% in bending angle of 1080°, and the rotation torsional moment by mechanics test reached 5 N·μm. Consequently, monolayer design realized complex chiral torsion much easier than those tedious reciprocating scanning strategies, showcasing no mechanical mismatch or breaking.

To spatiotemporally program reconfiguration at specific sites, we accurately manipulated a buckling action by varying NWs' density at segmented regions. Low-density regions preferentially buckled upward due to unfoldable space (Figure S7, the buckled area elevated over 7 μm at altitude). The compact area was anchored on the substrate and coordinated with the smoothly crosslinked area to regulate the buckling duty cycle, forming a freestanding arch bridge landscape (Figure 3F1 and F2). In 3D micrographs, the loose interspacing region buckled out-plane and was evidenced by laser scanning confocal microscopy (LSCM, LEXT OLS5000™, Olympus) cross-sectional view to evaluate profile at sub wavelength accuracy. The as-demonstrated reversible 2D-to-3D transforming geometries at different freedom or positions all started from the same planar shape.

Holding or gripping motion meant an indispensable function in microfluidics applications or intravascular surgery[12,46]. For creating monolayer biomimetic hands or grippers, we divided MNIH structural design accordingly, scanning at different directions and densities. As seen in

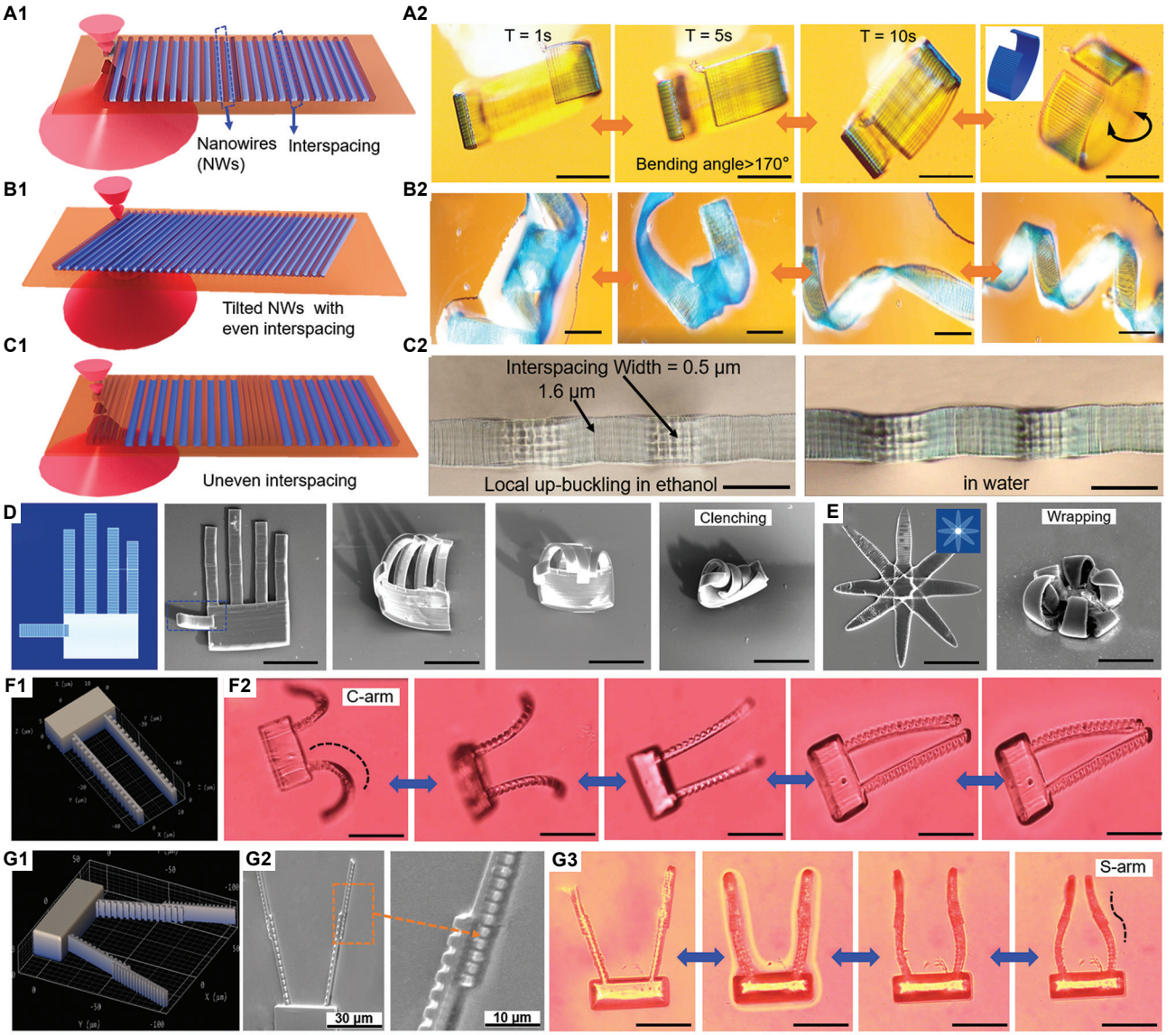

Figure 3. The accumulated intermolecular force realized higher freedom responsiveness. (A_1 and A_2) Here, a series of CCD photographs show that MNIH transformed into a "bracelet" shape that brook the constraint at the x-y plane. The scale bar is 50 μm. (B_1 and B_2) Titling-nanowires made MNIH crimp into a dynamic chiral torsion at three turns reversely. (C_1 and C_2) A specific-sited landscape like an arch bridge self-buckled up from the same planar shape with (A) and (B) (but with different densities) due to uneven swelling degrees in an ethanol/water solution. (D) SEM images of as-prepared four hand-mimic MNIHs curling into a clenched fist by heating without water or liquid. (E) A heat-depended flower-mimic MNIHs, acting like a sensitive mimosa. The scale bar in (D) and (E) is 50 μm. (F_1, and F_2) Models and SEM images of an in-plane griper-mimic MNIH bent at a C shape. The scale bar is 50 μm. (G_1-G_3) Another soft-interactive gripper with a pair of S-shaped arms. The scale bar of CCD micrographs is 50 μm

SEM images of dexterous five-finger palms (Figure 3D), the thumb spontaneously bent at the horizontal axis, and the other fingers bent following until finally clenched into a fist by gradient heating. Then, we programmed a dynamic apricot flower-mimic MNIH (Figure 3E), where six petals were scanned in a tangent direction accordingly. Therefore, all petals bent out-plane orientating to the same center under stimuli without compound layers, and the closure action represented an out-plane gripper readily for capturing tiny particles or cells. With more rational designs, fsLDW certainly promised more highly-directional out-plane mutation for gripping function.

To optimize local shape-programmability, we proposed a gear teeth-like geometry to the design, which generated asymmetric distribution of intermolecular force along the gripper's arm for higher-degree controllability in bending degree. The fsLDW's flexibility allowed to change the

number and location of the gear teeth structures, promising a novel ability to choose the stimuli interaction type beyond 4D programmability. The as-fabricated gripper MNIH bent its arms with asymmetric gear teeth from a typical C-arm (Figure 3F2 and Video clip S3) to a higher-freedom S-arm (Figure 3G1-G3, the arm bent in shifting directions to form S-shape closure/opening actions). Noticeably, we not only modified the arm bending configuration, but also selected the actuation conditions simultaneously as observed. C-armed gripper (Figure 3F2) was closed by absorbing solvent, and in contrast, the S-arm gripper (Figure 3G2 and G3) opened under the same condition, and was closed by evaporating solvent. Therefore, the gear teeth arrangement allowed MNIHs to select actuation stimuli, bringing the simple shape-reconfiguration to a higher level.

After investigations were done considering MNIHs as mechanically-interconnect devices, we identified the shape reconfiguration of the nanometric unit, NWs, which was the cornerstone for reprogrammed behavior (Figure 4). As described, TPP provided sub-200 nm line width and sub-10 nm surficial roughness (Figure S8) of NWs to exceed the optical diffraction limits[8,41], therefore promising novel hydrogel-nature photonic crystal applications based on nanowire structure. We separated NWs (without interconnection) for interactive PCs with gradient structure coloration. A riot of tunable coloration was realized for micro-scale anti-counterfeiting marks, optical information storage, or display (Figures 1, 4A and B). Their periodic structure became dynamic because hydrogel NWs slightly swelled or shrunk to modulate its dielectric constant difference by the changeable solvent retention, tuning the photonic band gap[40,47] as multi-stage photon filters.

We further found a light-deformable ability of the PEG/NIPAM/TAIC network inside MNIHs, which modulated the local internal stress like photon-active muscles" for clarity. The remote laser-irradiated local region thermally expanded according to the applied light. As evidence, a fabricated free-standing frog-mimicking MNIH (dimension $<100 \times 100 \times 40$ μm^3) became photoactive[48] but without liquid crystal elastomer (Figure S9), showing the hybrid PEG/NIPAM/TAIC network as alternative photon-active materials. Photon-thermal conversion redistributed the swelling-induced stress of the frog head, making the frog nod continuously (Videoclip S4) at a frequency and amplitude relying on the laser radiation without fatigue over 10^4 actuation cycles.

In potential bio-chip applications[49] such as medical theranostics, or regenerative engineering, the biocompatibility and human-friendliness of using MNIHs are matters of concern[50,51]. To verify cytotoxicity, the as-prepared MNIH samples were rinsed, disinfected, and loaded with fibroblasts for viability evaluations with the live-dead assay kit. Fluorescence microscopy images reflected the cell-culturing activities on MNIHs. Fibroblasts[51] spread (stained in green, Figure 4C) throughout the surfaces of the MNIHs with desirable adhesion. The constantly-high cell viability values across the entire culture period (Figure 4B, >97.55%) suggested the availability of MNIHs as implantable bio-robotics or medical care.

For actual usage, we need to investigate the self-repairing[52-58] ability under extreme conditions. As known, hydrogel nature bestowed MNIHs with an impact/shock-absorbing ability superior to those non-deformable constructs, as plastic or metal structures were usually decomposed into pieces if being deformed. To check this ability in room conditions, we implemented a series of damage experiments on MNIHs. After being intentionally poked or squeezed by externally-applied forces, MNIHs would not disintegrate, instead, these damaged MNIHs spontaneously recovered (Figure 4F and G, the small organic molecules PEG-400 penetrated MNIH as a mobile nano binder to automatically stitch up wounds), displaying self-repairing function under harsh environments such as accidental shock or destruction. For instance, a micro-structured "broken heart" MNIH (Figure 4F) self-fixed itself after an intentional distortion caused by squeezing with the use of a hard tweezer. The "broken heart" MNIH self-repaired and returned to the pre-designed symmetrical shape simply by absorbing PEG-400 molecules (structural similarity over 90%, Video clip S5), and avoided turning into waste after accidental damage. The reconstructed stiffness/Young's modulus reached over 70% of the initial state. Beneficially, no tedious surgical operation/diagnosis, fixation, or tools were necessary through the self-repairing process.

To in-depth verify the recovering ability, we forcibly poked an MNIH woodpile using a sharp needle, leaving behind two through holes. Strikingly, the physically-damaged hole absorbed PEG-400 molecules, and regenerated the pre-designed woodpile structure without guidance, showcasing a typical shape-memory characteristic. As shown, the damaged area exposed more functional groups to capture organic (PEG-400) molecules than the other areas. The strength of the intermolecular interaction between binder and MNIHs determined the recovered strength. As confirmed, MNIHs possessed shape-memory characteristics, enabling the recovery process to happen toward the initial design, not to an amorphous form.

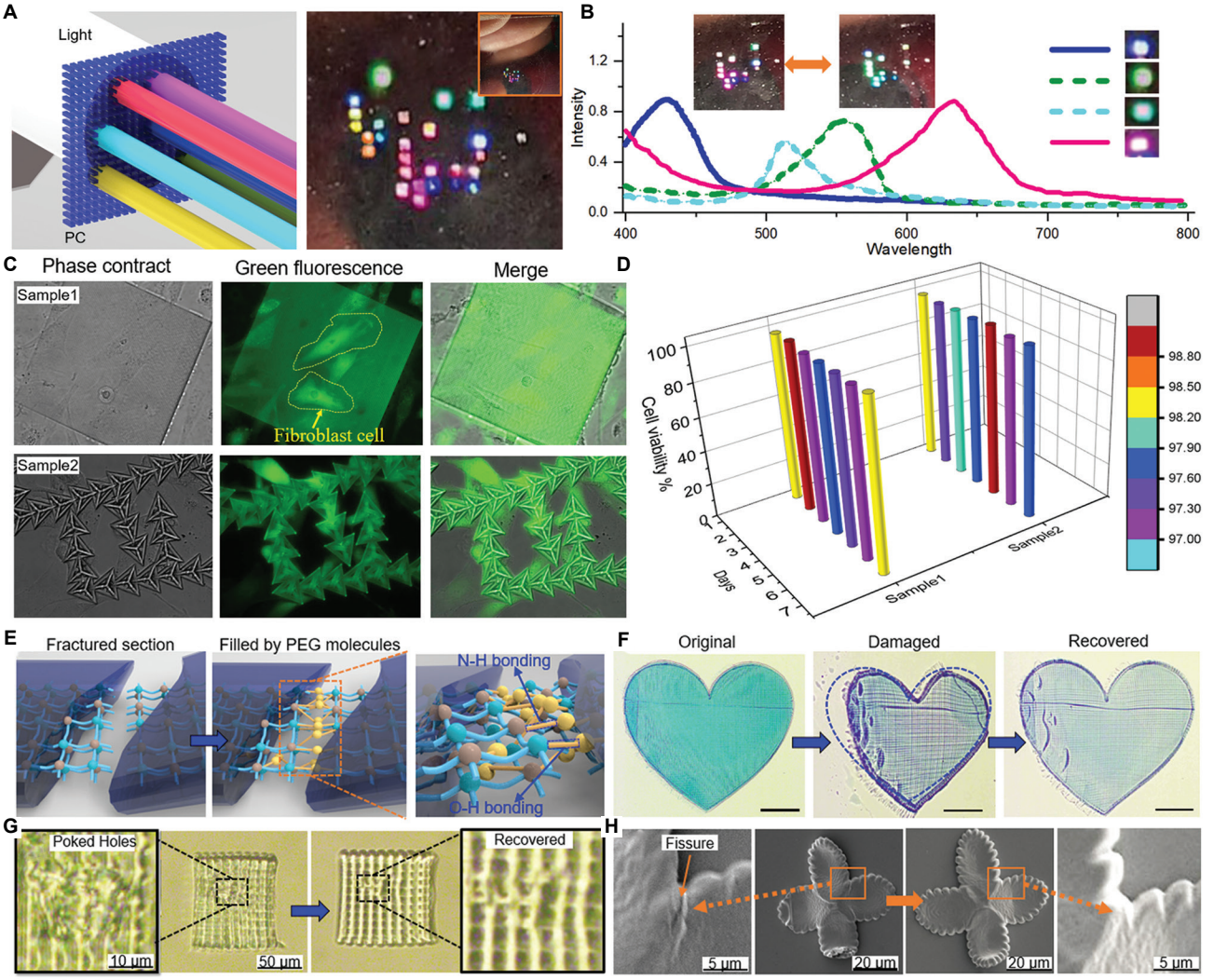

Figure 4. (A) Tunable photon filtering from a white light source using the MNIH PCs, color shifted as the CCD images. (B) The visibly-highlighted structural coloration and transmission spectra of PCs, and spectral characters matched well with the microscale footprint coloration. (C) Phase image, fluorescence image, and merged image of the tested MNIHs in cell cytotoxicity test. Sample 1 was a single-layer PC, and sample 2 was an array of hollow hexahedrons, where the pencil-shape fibroblast cells were crawling on hydrogel block. (D) Cell viability summary of Figure 3C across 1 week on MNIHs. Both samples maintained cell viability ratio of over 95%. (E) The mechanism of self-assembling PEG molecules for repairing damaged fissures. (F) An impaired heart-shaped MNIH self-recovered to its initial symmetric shape. (G) A poked hole in planar MNIHs absorbed PEG-400 molecules to reconstruct the damaged areas, confirming the highly-valuable autonomic repairing process. (H) A similar self-healing process could be found in other mechanically-damaged flower-shaped MNIHs with the aid of PEG-400

4. Conclusions

Based on the investigation described in the above, we first confirmed that the monolayer heterojunction scanning strategy promised an unimaginable capacity of μ/n scale, high-controllable shape reconfiguration for actual requirements. Then, this method exhibited superior advantages over the orthodox 3D printing in a few aspects:

(i) Basically, the flexible fsLDW incorporating interactives hydrogels inherited the materials' potential (amphipathic, soft mechanics, self-adaptiveness to small loads of stimuli), and maximized it substantially at nanometer precision. As exhibited, the reverse molecular interaction and the resultant stretching and contracting all become tunable at the basic unit of single nanowires (the most precise programming unit at least three-order smaller than the reported 3D-printed robotics) for the first time.

(ii) Subsequently, multiple reconfigurations in one starting shape now became accessible by proper design, which promised more mechanical mutations to μ/n robotics for complex functions. Many other

biomimetic features were realized or systematically integrated on-chip through our method with better chiral torsion, gripping, or smart photonics as demonstrated.

(iii) Furthermore, the satisfactory cytocompatibility and cell-adhesive properties are ascribed to the hydrogel nature of the PEG and NIPAM in the composite network. The measured cell viability and desirable adhesion behavior proved MNIHs' readiness for the increasing market of bio-environmental applications.

(iv) Experiments confirmed the molecule-level interaction is self-driven without any batteries, electric motors, or pneumatic systems. The non-covalent effect underneath interaction leads to a revolutionary μ/n scale transformation between mechanical energy and chemical energy.

(v) Moreover, we unexpectedly found that the impaired MNIHs automatically recovered to initial shape like having self-consciousness without an in-built diagnosis or sensing parts, implying desirable device longevity in exposure to the outside-applied impact, which outperformed the existing robots or 3D-printed products which could turn into waste if deformed or broken.

In a nutshell, we proposed a novel, ultrafast laser 4D bioprinting method. For verification, we designed, fabricated, and identified the versatility of the programmed interactive μ/n scale hydrogels. The release principle and biomimetic ability lay a solid foundation for innovative development of hydrogels. The as-exhibited self-driven grippers/artificial hands, photon filters, and transformers exclusively exhibited high shape programmability, high biocompatibility, and high fatigue resistance in the absence of troublesome mechanical mismatching issues of the previous dual/tri-layer design.

Acknowledgments

All authors were grateful to Prof. Xiong Wei, Dr. Deng Cunsan, and Dr. Fan Xuhao of Huazhong University of Science and Technology for their support and guidance.

Funding

This research was financially supported by the National Key R&D Program of China (SQ2018YFB110138), National Science Youth Fund of China (61805094), Natural Science Foundation of Jiangsu (BK20221363, BK20210746), and China Postdoctoral Science Foundation (2017M622417).

Conflict of interest

The authors declare that they have no conflict of interest.

Author contributions

Conceptualization: Yufeng Tao
Investigation: Yufeng Tao, Zhiduo Xin, Xia Cao
Methodology: Chengchangfeng Lu
Validation: Xuejiao Wang
Writing – original draft: Yufeng Tao
Writing – review & editing: Yunpeng Ren

Ethics approval and consent to participate

Not applicable.

Consent for publication

All authors approved the final manuscript and the submission to this journal.

Availability of data

All data supporting this study are available in the supplementary material of this article.

References

1. Sun HL, Klok HA, Zhong ZY 2018, Polymers from nature and for nature. *Biomacromolecules*, 19: 1697–1700.

https://doi.org/10.1021/acs.biomac.8b00830

2. Xu F, Fu CB, Yang YF, 2020, Water affects morphogenesis of growing aquatic plant leaves. *Phys Rev Lett,* 124: 038003.

https://doi.org/10.1103/physrevlett.124.038003

3. Liang H, Mahadevan L, 2011, Growth, geometry, and mechanics of a blooming lily. *Proc Natl Acad Sci*, 108: 5516–5521.

https://doi.org/10.1073/pnas.1007808108

4. Hu Y, Wang Z, Jin D, *et al.*, 2019, Botanical-inspired 4D printing of hydrogel at the microscale. *Adv Funct Mater,* 30: 1907377.

https://doi.org/10.1002/adfm.201907377

5. Miao SD, Castro N, Nowicki M, *et al.,* 2017, 4D printing of polymeric materials for tissue and organ regeneration. *Mater Today,* 20: 577–591.

https://doi.org/10.1016/j.mattod.2017.06.005

6. Bastola A, Rodriguez NJ, Behl M, *et al.*, 2021, Cactus-inspired design principles for soft robotics-based on 3D printed hydrogel-elastomer systems. *Mater Design*, 202: 109515.

https://doi.org/10.1016/j.matdes.2021.109515

7. Almeida AC, Canejo J, Fernandes S, *et al.*, 2018, Cellulose-based biomimetics and their applications. *Adv Mater,* 30: 1703655.

https://doi.org/10.1002/adma.201703655

8. Jeong HY, Lee E, An S, *et al.*, 2020, 3D and 4D printing for

optics and metaphotonics. *Nanophotonics,* 9: 1139–1160.

https://doi.org/10.1515/nanoph-2019-0483

9. Wang S, Lee JM, Yeong WY, 2015, Smart hydrogels for 3D bioprinting, *Int J Bioprint,* 1: 01005.

10. Apsite I, Biswas A, Li Y, *et al.*, 2020, Microfabrication using shape-transforming materials. *Adv Funct Mater,* 30: 1908028.

https://doi.org/10.1002/adfm.201908028

11. Gladman AS, Matsumoto EA, Nuzzo RG, *et al.*, 2016, Biomimetic 4D printing, *Nat Mater,* 15: 413–418.

https://doi.org/10.1038/nmat4544

12. Son H, Byun E, Yoon YJ, *et al.*, 2020, Untethered actuation of hybrid hydrogel gripper via ultrasound. *ACS Macro Lett,* 9: 1766–1772.

https://doi.org/10.1021/acsmacrolett.0c00702

13. Visentin F, Babu SP, Meder F, *et al.*, 2021, Selective stiffening in soft actuators by triggered phase transition of hydrogel-filled elastomers. *Adv Funct Mater,* 31: 2101121.

https://doi.org/10.1002/adfm.202101121

14. Mishra AK, Pan WY, Giannelis E, *et al.,* 2021, Making bioinspired 3D-printed autonomic perspiring hydrogel actuators. *Nat Protoc,* 16: 2068–2087.

https://doi.org/10.1038/s41596-020-00484-z

15. Adam G, Benouhiba A, Rabenorosoa K, *et al.*, 2021, 4D printing: Enabling technology for microrobotics applications. *Adv Intell Syst,* 3: 2000216.

https://doi.org/10.1002/aisy.202000216

16. McLellan K, Sun YC, Naguib H, 2022, A review of 4D printing: Materials, structures, and designs towards the printing of biomedical wearable devices. *Bioprinting,* 27: e00217.

https://doi.org/10.1016/j.bprint.2022.e00217

17. Xing J, Zheng M, Duan X, 2015, Two-photon polymerization microfabrication of hydrogels: An advanced 3D printing technology for tissue engineering and drug delivery. *Chem Soc Rev*, 44: 5031–5039.

https://doi.org/10.1039/c5cs00278h

18. Jin DD, Chen QY, Huang T, *et al.*, 2020, Four-dimensional direct laser writing of reconfigurable compound micromachines. *Mater Today,* 32: 19–25.

https://doi.org/10.1016/j.mattod.2019.06.002

19. Gardi G, Ceron S, Wang W, *et al.,* 2022, Microrobot collectives with reconfigurable morphologies, behaviors, and functions. *Nat Commun,* 13: 2239.

https://doi.org/10.1038/s41467-022-29882-5

20. Zhuo SY, Zhao ZG, Xie ZX, *et al.,* 2020, Complex multiphase organohydrogels with programmable mechanics toward adaptive soft-matter machines. *Sci Adv,* 6: eaax1464.

https://doi.org/10.1126/sciadv.aax1464

21. Zhao Z, Kuang X, Yuan C, *et al.,* 2018, Hydrophilic/hydrophobic composite shape-shifting structures. *ACS Appl Mater Interf*, 10: 19932–19939.

https://doi.org/10.1021/acsami.8b02444

22. Wu Y, Hao X, Xiao R, *et al.,* 2019, Controllable bending of bi-hydrogel strips with differential swelling. *Acta Mech Solida Sin,* 32: 652–662.

https://doi.org/10.1007/s10338-019-00106-6

23. Van Hoorick J, 2017, Cross-linkable gelatins with superior mechanical properties through carboxylic acid modification: Increasing the two-photon polymerization potential. *Biomacromolecules,* 18: 3260–3272.

https://doi.org/10.1021/acs.biomac.7b00905

24. Urrios A, Parra-Cabrera C, Bhattacharjee N, *et al.*, 2016, 3D-printing of transparent bio-microfluidic devices in PEG-DA. *Lab Chip,* 16: 2287–2294.

https://doi.org/10.1039/c6lc00153j

25. Dey R, Mukherjee R, Haldar J, 2022, Photo-crosslinked antimicrobial hydrogel exhibiting wound healing ability and curing infections *in vivo*. *Adv Healthc Mater,* 5: 2224–2231.

https://doi.org/10.1002/adhm.202200536

26. Ceylan H, Yasa IC, Yasa O, *et al.,* 3D-printed biodegradable microswimmer for theranostic cargo delivery and release. *ACS Nano,* 13: 3353–3362.

https://doi.org/10.1021/acsnano.8b09233

27. Tao YF, Lu CC, Deng CS, *et al.,* 2022, Four-dimensional stimuli-responsive hydrogels micro-structured via femtosecond laser additive manufacturing. *Micromachines,* 13: 32.

https://doi.org/10.3390/mi13010032

28. Bauhofer AA, Krödel S, Rys J, *et al.*, 2017, Harnessing photochemical shrinkage in direct laser writing for shape morphing of polymer sheets. *Adv Mater,* 29: 1703024.

https://doi.org/10.1002/adma.201703024

29. Zhang F, Lian MY, Alhadhrami A, *et al.*, 2022, Laccase immobilized on functionalized cellulose nanofiber/alginate composite hydrogel for efficient bisphenol A degradation from polluted water. *Adv Compos Hybrid Mater*, 5: 1852–1864.

https://doi.org/10.1007/s42114-022-00476-5

30. Kong D, EI-Bahy ZM, Algadi H, *et al.*, 2022, Highly sensitive strain sensors with wide operation range from strong MXene-composited polyvinyl alcohol/sodium carboxymethylcellulose double network hydrogel. *Adv Compos Hybrid Mater*, 5: 1976–1987.

https://doi.org/10.1007/s42114-022-00531-1

31. Wu YF, Chen EF, Weng XD, *et al.*, 2022, Conductive polyvinyl alcohol/silver nanoparticles hydrogel sensor with large draw ratio, high sensitivity and high stability for human behavior monitoring. *Eng Sci*, 18: 113–120.

32. Huang K, Wu YF, Liu JC, *et al.*, 2022, A double-layer carbon nanotubes/polyvinyl alcohol hydrogel with high stretchability and compressibility for human motion detection. *Eng Sci*, 17: 319–327.

33. Tao YF, Wei CY, Liu JW, *et al.*, 2019, Nanostructured electrically conductive hydrogels via ultrafast laser processing and self-assembly. *Nanoscale*, 11: 9176–9184.

https://doi.org/10.1039/c9nr01230c

34. Yamamoto Y, Kanao K, Arie T, *et al.*, 2015, Air ambient-operated pNIPAM-based flexible actuators stimulated by human body temperature and sunlight. *ACS Appl Mater Interf,* 7: 11002–11006.

https://doi.org/10.1021/acsami.5b02544

35. Forg S, Karbacher A, Ye ZS, *et al.*, 2022, Copolymerization kinetics of dopamine methacrylamide during PNIPAM microgel synthesis for increased adhesive properties. *Langmuir,* 38: 5275–5285.

https://doi.org/10.1021/acs.langmuir.1c02749

36. Wolski L, Ziolek M, 2018, Insight into pathways of methylene blue degradation with H2O2 over mono and bimetallic Nb, Zn oxides. *Appl Catal B Environ,* 224: 634–647.

https://doi.org/10.1016/j.apcatb.2017.11.008

37. Fernández-Pérez A, Marbán G, 2022, Visible light spectroscopic analysis of methylene blue in water. *J Appl Spectrosc,* 88: 1284–1290.

https://doi.org/10.1007/s10812-022-01310-y

38. Özcan M, Cakmakci M, Temize İ, 2020, Smart composites with tunable stress-strain curves. *Comput Mech,* 65: 375–394.

https://doi.org/10.1007/s00466-019-01773-5

39. Yang LX, Yang LB, Lowe RL, 2021, A viscoelasticity model for polymers: Time, temperature, and hydrostatic pressure dependent Young's modulus and Poisson's ratio across transition temperatures and pressures. *Mech Mater,* 157: 103839.

https://doi.org/10.1016/j.mechmat.2021.103839

40. Tao YF, Deng CS, Long J, *et al.,* 2022, Multiprocess laser lifting-off for nanostructured semiconductive hydrogels. *Adv Mater Interf,* 9: 2101250.

https://doi.org/10.1002/admi.202101250

41. Tao YF, Ren YP, Wang XJ, *et al.,* 2021, A femtosecond laser-assembled SnO2 microbridge on interdigitated Au electrodes for gas sensing. *Mater Lett*, 308: 131120.

https://doi.org/10.1016/j.matlet.2021.131120

42. Hua J, Björling M, Larsson R, *et al.*, 2022, Friction control of chitosan-Ag hydrogel by silver ion. *ES Mater Manuf,* 16: 30–36.

43. Kordjazi S, Kamyab K, Hemmatinejad N, 2020, Super-hydrophilic/oleophobic chitosan/acrylamide hydrogel: An efficient water/oil separation filter. *Adv Compos Hybrid Mater*, 3: 167–176.

https://doi.org/10.1007/s42114-020-00150-8

44. Zhao WW, Chen LJ, Hu SM, *et al.*, 2020, Printed hydrogel nanocomposites: Fine-tuning nanostructure for anisotropic mechanical and conductive properties. *Adv Compos Hybrid Mater*, 3: 315–324.

https://doi.org/10.1007/s42114-020-00161-5

45. Wang TR, Wusigale, Kuttappan D, *et al.*, 2021, Polydopamine-coated chitosan hydrogel beads for synthesis and immobilization of silver nanoparticles to simultaneously enhance antimicrobial activity and adsorption kinetics. *Adv Compos Hybrid Mater,* 4: 696–706.

https://doi.org/10.1007/s42114-021-00305-1

46. Liu Z, Wang Y, Ren YY, *et al.,* 2020, Poly(ionic liquid) hydrogel-based anti-freezing ionic skin for a soft robotic gripper. *Mater Horiz,* 7: 919–927.

https://doi.org/10.1039/c9mh01688k

47. Zhang Y, Le X, Jian Y, *et al.,* 2019, 3D fluorescent hydrogel origami for multistage data security protection. *Adv Funct Mater,* 29: 1905514.

https://doi.org/10.1002/adfm.201905514

48. Zhu QY, Du C, Dai YH, *et al.,* 2020, Light-steered locomotion of muscle-like hydrogel by self-coordinated shape change and friction modulation. *Nat Commun,* 11: 5166.

https://doi.org/10.1038/s41467-020-18801-1

49. Capella V, Rivero R, Liaudat A, *et al.*, 2019, Cytotoxicity and bioadhesive properties of poly-N-isopropylacrylamide hydrogel. *Heliyon,* 5: e01474.

https://doi.org/10.1016/j.heliyon.2019.e01474

50. Urzedo AL, Gonçalves MC, Nascimento MH, *et al.,* 2020, Cytotoxicity and antibacterial activity of alginate hydrogel containing nitric oxide donor and silver nanoparticles for topical applications. *ACS Biomater Sci Eng,* 6: 2117–2134.

https://doi.org/10.1021/acsbiomaterials.9b01685

51. Mölzer C, Shankar SP, Masalski V, *et al.*, 2019, TGF-β1-activated Type 2 dendritic cells promote wound healing and induce fibroblasts to express Tenascin C following corneal full-thickness hydrogel transplantation. *J Tissue Eng Regen Med,* 13: 1507–1517.

https://doi.org/10.1002/term.2853

52. Ma XY, Zhong W, Zhao J, *et al.*, 2020,"Self-heating" enabled one-pot synthesis of fluorescent carbon dots. *Eng Sci*, 9: 44–49.

53. Zhao L, Tallman T, Lin G, 2021, Spatial damage characterization in self-sensing materials via neural network-aided electrical impedance tomography: A computational study. *ES Mater Manuf*, 12: 78–88.

https://doi.org/10.30919/esmm5f919

54. Song TT, Jiang BJ, Li YD, *et al*., 2021, Self-healing materials: A review of recent developments. *ES Mater Manuf*, 14: 1–19.

55. Sun DW, Yan JH, Ma XU, *et al*., 2021, Tribological investigation of self-healing composites containing metal/polymer microcapsules. *ES Mater Manuf*,14: 59–72.

56. Zhang DJ, Wang XY, He YX, *et al*., 2022, Self-restoration of underwater low adhesive superoleophobicity on shape memory polymer arrays. *Eng Sci*, 17: 343–50.

57. Chen F, Xiao H, Peng ZQ, *et al*., 2021, Thermally conductive glass fiber reinforced epoxy composites with intrinsic self-healing capability. *Adv Compos Hybrid Mater*, 4: 1048–1058.

https://doi.org/10.1007/s42114-021-00303-3

58. Liu C, Yin Q, Li X, *et al*., 2021, A waterborne polyurethane-based leather finishing agent with excellent room temperature self-healing properties and wear-resistance. *Adv Compos Hybrid Mater*, 4: 138–149.

https://doi.org/10.1007/s42114-021-00206-3